CrossMark

Effect of Strain Rate on Deformation Behavior of AlCoCrFeNi High-Entropy Alloy by Nanoindentation

L. Tian, Z.M. Jiao, G.Z. Yuan, S.G. Ma, Z.H. Wang, H.J. Yang, Y. Zhang, and J.W. Qiao

In this study, nanoindentation tests with continuous stiffness measurement technique were measured to investigate the deformation behavior of a high-entropy alloy AlCoCrFeNi under different indentation strain rates at room temperature. Results suggest that the creep behavior exhibits remarkable strain rate dependence. In-situ scanning images showed a conspicuous pileup around the indents, indicating that an extremely localized plastic deformation occurred during the nanoindentation. Under different strain rates, elastic modulus basically remains unchanged, while the hardness decreases with increasing indentation depth due to the indentation size effect. Furthermore, the modulus and hardness of AlCoCrFeNi HEAs are greater than that of the $Al_xCoCrFeNi$ ($x = 0.3, 0.5$) at the strain rate of 0.2 s^{-1} due to its higher negative enthalpy of mixing related to the atomic binding force, and the solid solution strengthening induced by the lattice distortion, respectively.

1. Introduction

As a new class of materials, high-entropy alloys (HEAs) have received increasing attention in the last decade (Ref 1-4). HEAs are multi-principal component alloys, which are composed of at least five equiatomic or near equiatomic alloying elements (Ref 4). It is interesting to be noted that HEAs mostly tend to form simple face-centered cubic (FCC) and/or body-centered cubic (BCC) solid solutions rather than intermetallics or complex phases, which is often attributed to a high configuration entropy of mixing (Ref 5, 6). Moreover, high-entropy alloys with hexagonal close-packed (HCP) structure based on rare earth elements also has been proposed and studied recently, which is very important for further under-

L. Tian, Z.M. Jiao, and Z.H. Wang, Institute of Applied Mechanics and Biomedical Engineering, Taiyuan University of Technology, Taiyuan 030024, People's Republic of China; and Shanxi Key Laboratory of Material Strength and Structure Impact, Taiyuan University of Technology, Taiyuan 030024, People's Republic of China; G.Z. Yuan, S.G. Ma, and J.W. Qiao, Institute of Applied Mechanics and Biomedical Engineering, Taiyuan University of Technology, Taiyuan 030024, People's Republic of China; H.J. Yang, Laboratory of Applied Physics and Mechanics of Advanced Materials, College of Materials Science and Engineering, Taiyuan University of Technology, Taiyuan 030024, People's Republic of China; and Y. Zhang, State Key Laboratory for Advanced Metals and Materials, University of Science and Technology Beijing, Beijing 100083, People's Republic of China. J.W. Qiao, Institute of Applied Mechanics and Biomedical Engineering, Taiyuan University of Technology, Taiyuan 030024, People's Republic of China; and Laboratory of Applied Physics and Mechanics of Advanced Materials, College of Materials Science and Engineering, Taiyuan University of Technology, Taiyuan 030024, Peoples Republic of China. Contact e-mails: tianlin1129@yahoo.com, wangzh@tyut.edu.cn and qiaojunwei@gmail.com.

standing HEA formation mechanisms (Ref 7). Due to the different atomic sizes and chemical bonds of the constituent elements, HEAs often possess a highly distorted lattice structure which leads to a high strength caused by solid solution hardening (Ref 8-10). Many fascinating and excellent properties exist in HEAs, such as high yielding strength (Ref 2), and superior hardness (Ref 11-13), and outstanding thermal stability (Ref 14), as well as good corrosion resistance (Ref 2), which are of much importance for functional and structural applications (Ref 4, 15). Hence, HEAs have great potential to be widely utilized in different aspects. For instance, HEAs are often applied as coating materials in the high-temperature environment (Ref 15).

Current HEAs are typically based upon the transition metals Cr, Co, Fe, Ni, Mn, and Cu or on refractory metals such as V, Cr, Ti, Mo, Nb, Ta, W, Zr, and Hf (Ref 4, 16). The compound forming elements Al and Ti are often added to both families (Ref 17). Recently, the $Al_xCoCrFeNi$ HEA system has been studied and characterized for their microstructure and properties. In particular, Wang et al (Ref 18) investigated the microstructure and mechanical property of as-cast $Al_xCoCrFeNi$ high-entropy alloy with finely divided Al contents and found that the increase of Al addition leads to the formation of BCC structure which is the main hardening factor. Jiao et al (Ref 19) comparatively studied the mechanical properties of $Al_{0.3}CoCrFeNi$ & AlCoCrFeNi in nanoindentation by controlling indentation loading rates (Ref 19), finding that the P-h curves of the two HEAs exhibited apparent discontinuities at low loading rates and the increase of Al concentration has a significant effect on the mechanical behaviors of the two alloys. In addition, Wang et al (Ref 12) studied the mechanical properties of AlCoCrFeNi HEA with BCC structure and observed that the alloy exhibited high yielding strength and large plastic deformation upon compression at the strain rate of 5×10^{-4} s^{-1}. However, with regard to the strain rate sensitivity via controlling the strain rates, limited studies on the mechanical properties and deformation behavior of the AlCoCrFeNi HEA were reported at micro- or nano-scales.

To date, nanoindentation is one of the most booming technologies to study the mechanical properties of small-sized

samples (Ref 15). The material hardness and modulus have been well measured during nanoindentation tests (Ref 20, 21). Meanwhile, methods have also been proposed for evaluating other mechanical parameters, including the hardening exponent (Ref 22), creep parameter, and residual stresses (Ref 23). Jiao et al (Ref 19) studied the mechanical properties of $Al_{0.3}CoCrFeNi$ & AlCoCrFeNi in nanoindentation by controlling indentation loading rates, finding the P-h curves of the two HEAs exhibited apparent discontinuities at low loading rates and the increase of Al concentration has a significant effect on the mechanical behaviors of the two alloy. So our paper is based on their works. We investigated the deformation behavior of AlCoCrFeNi HEA under different indentation strain rates. We have described the relationship between our paper with aforementioned studies in the second paragraph of Introduction Section. So in the last paragraph of Introduction, we emphasized the significance of our paper instead of introducing the aforementioned works in detail.

2. Experimental

2.1 Samples Preparation

Cylindrical rods of the AlCoCrFeNi alloy were prepared by arc melting pure elements with a high purity (99.99%) under a high purified argon atmosphere. The ingots were then remelted four times in order to obtain chemical homogeneity. The samples with a diameter of 3 mm were obtained by injecting cast into a water-cooled copper mold. The microstructure was examined by scanning electron microscope (SEM) equipped with energy dispersive spectrometer (EDS). Before nanoindentation tests, the surface of samples was mechanically polished to a mirror finish.

2.2 Nanoindentation Tests

Nanoindentation tests were performed at room temperature on Agilent Nano Indenter G200 with a Berkovich diamond tip, before which initial machine calibration was conducted on standard fused silicon to improve the accuracy of measurement data. The displacement and load resolutions of the machine were 0.01 nm and 50 nN, respectively. Thermal drift correction of the machine dropped down to 0.05 nm/s to remove the thermal drift effect. The Poisson's ratio was settled to be 0.25. The indenter was held for 10 s during the holding stage to determine whether a creep behavior occurred. The 20 μm interval is chosen to avoid overlap of plastic zones created by neighboring indentations. Furthermore, the reliability of the results is verified by conducting at least five independent experiments at each testing condition.

Indentation tests for the AlCoCrFeNi alloy are carried out with four different indentation strain rates of 0.002, 0.02, 0.2, and 0.5 s^{-1} under 1000 nm depth limitation in order to study strain rate sensitivity and ISE in nanohardness. In addition, based on the continuous stiffness measurement (CSM) technique, the elastic modulus and hardness can be continuously obtained during loading (Ref 25-27). After nanoindentations, the images around the indents are immediately obtained using in-situ scanning system.

According to the paper by Oliver et al. (Ref 24), the indentation strain rate, $\dot{\varepsilon}_i$, can be defined as the instantaneous displacement rate of the indented divided by the instantaneous displacement $\left(\dot{\varepsilon}_i = \frac{1}{h}\frac{dh}{dt}\right)$. Indentation loading rate is defined as $\dot{P} = \frac{dp}{dt}$, where P is the applied load. A relationship between the indentation strain rate $\dot{\varepsilon}_i$ and indentation loading rate $\dot{P}$ can be established, as described in the following equation:

$$\dot{\varepsilon}_i = \frac{\dot{h}}{h} = \frac{1}{2}\frac{\dot{P}}{P}$$

Notwithstanding, the relationship between the indentation strain rate and indentation loading rate has ever been utilized to discuss the strain rate dependencies of materials, such as reference (Ref 19). As to material strain rate, it is the rate of change in strain (deformation) of a material with respect to time, defined as $\dot{\varepsilon} = \frac{d\varepsilon}{dt}$. In the traditional uniaxial test, the uniaxial strain rate of a material $\dot{\varepsilon}_u$ is the material strain rate. For nanoindentation tests, the indentation strain rate $\dot{\varepsilon}_i$ is the material strain rate. So material strain rate could be considered as a macroscopic concept which characterizes the mechanical properties of materials. Moreover, the indentation strain rate $\dot{\varepsilon}_i$ can be related to the uniaxial strain rate $\dot{\varepsilon}_u$ by $\dot{\varepsilon}_u = 0.09\dot{\varepsilon}_i$ (Ref 28). Furthermore, based on the study by Schuh et al. (Ref 29), indentation loading rate can be replaced by an approximate shear strain rate, $\dot{\gamma}_{eff}$. This was accomplished by first examining the indentation strain rate ($\dot{\varepsilon}_i = h^{-1} \cdot dh/dt$) of each experiment as done in (Ref 28), and identifying a reasonable average value; although $\dot{\varepsilon}_i$ actually varies as $1/h$ during a given test, it does level off to within about a factor of two after about the first 50 nm of travel. The effective shear strain rate is then related to the indentation strain rate by a constant ($\dot{\gamma}_{eff} \approx 0.16 \cdot \dot{\varepsilon}_i$) that incorporates (1) an approximate conversion from indentation to uniaxial strain rate (Ref 30), and (2) the usual $\sqrt{3}$ proportionality between uniaxial and shear strain rate. It is worth emphasizing that the strain rates we controlled in the present work to investigate the strain rate sensitivity are the indentation strain rates.
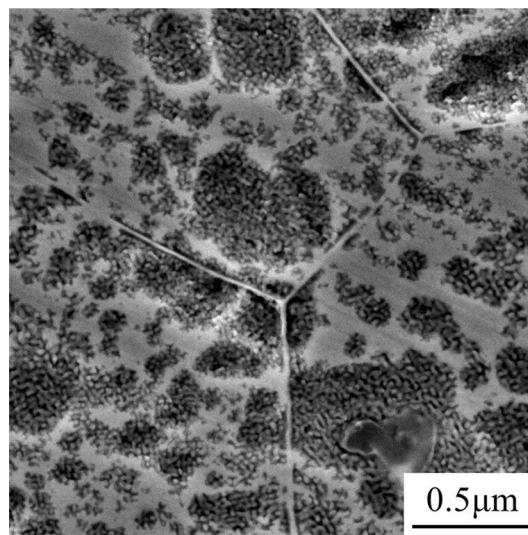
Fig. 1 SEM images of etched as-cast AlCoCrFeNi HEA, showing an equiaxed polycrystalline grain structure

3. Results and Discussion

Figure 1 shows the microstructure of the AlCoCrFeNi alloy. It is found that grain boundaries with about 120° intersection angle, typical of a polycrystalline structure, are observed in the as-cast sample. Furthermore, it is noted that a large amount of nanoscale precipitations, with an average size of about 50-100 nm, are intensively embedded on the grain matrix. Notwithstanding, the alloy with BCC structure is mainly composed of the mixture of A2 (disordered phase) and B2 (ordered phase), and may be a leaf phase in the as-cast condition. According to the investigation by Tang et al. (Ref 31) the as-cast AlCoCrFeNi alloy has a dendritic structure primarily consisting of a nano-lamellar mixture of A2 (disordered phase) and B2 (ordered phase) with almost the same lattice parameters, formed by the eutectic reaction, the dendrites with the volume fraction of 45% are enriched with Al and Ni, and the interdendritic regions with the volume fraction of 55% are enriched with Cr and Fe, while Co is uniformly distributed inside these phases.

Figure 2(a) exhibits the typical load-displacement curves under various strain rates with a depth limit of 1000 nm for the AlCoCrFeNi alloy. It should be noted that before the holding stage, the applied load becomes larger with increasing the strain rates under the same indentation displacement, demonstrating that the strain rate effect to the hardness of the AlCoCrFeNi alloy is available. It is worth emphasizing that even at the extremely small strain rate of 0.002 s^{-1}, the creep still appears during the holding stage (10 s), as shown in the set of Fig. 2(a). Compared with traditional uniaxial tensile/compressive creep tests, where the stress distribution is relatively homogeneous and normally without stress concentration, the stress contribution underneath the indenter is much more complicated (Ref 32). Unlike the traditional creep tests, the final failure of the sample does not occur during nanoindentation creep, when the maximum shear stress could surpass the yielding stress even at extremely shallow depth due to local shear deformation. That might be the intrinsic reason why the creep occurs in many high-melting point materials at room temperature by nanoindentation, whereas materials creep till the testing temperature is close to materials' melting point (Ref 15, 33, 34). Moreover, the creep behavior of the current alloy shows a strain rate dependence, which could be more clearly revealed between the creep displacement and holding time, as shown in Fig. 2(b). It is noted that the creep displacements and creep rates increase with increasing the strain rates. The strain rate dependence that creep displacement becomes larger with the strain rates could be attributed to the accumulation of visco-plastic deformation related to the dislocation dynamics under higher strain rates (Ref 35) and the transformation into larger creep deformation during the holding time (Ref 36). Furthermore, it can be observed that the creep curves captured during nanoindentation, as shown in Fig. 2(b), are very similar to the classic creep curves obtained in traditional creep tests except the failure stage, where the creep rate is accelerated and materials ultimately fail (Ref 15). Actually, the creep curves could be divided into two different stages as the transient and steady-state creeps. For simplicity, the transient creep is denoted as A, and the steady-state creep is denoted as B as exhibited in
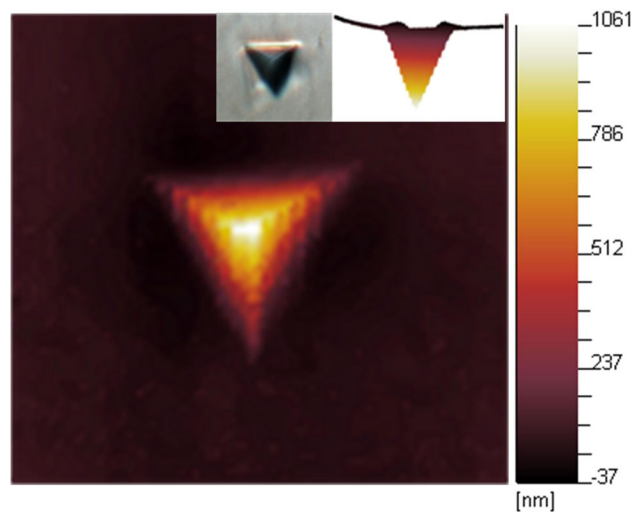

Fig. 3 In-situ scanning images after nanoindentation at an indentation strain rate of 0.02 s^{-1} with Berkovich indenter
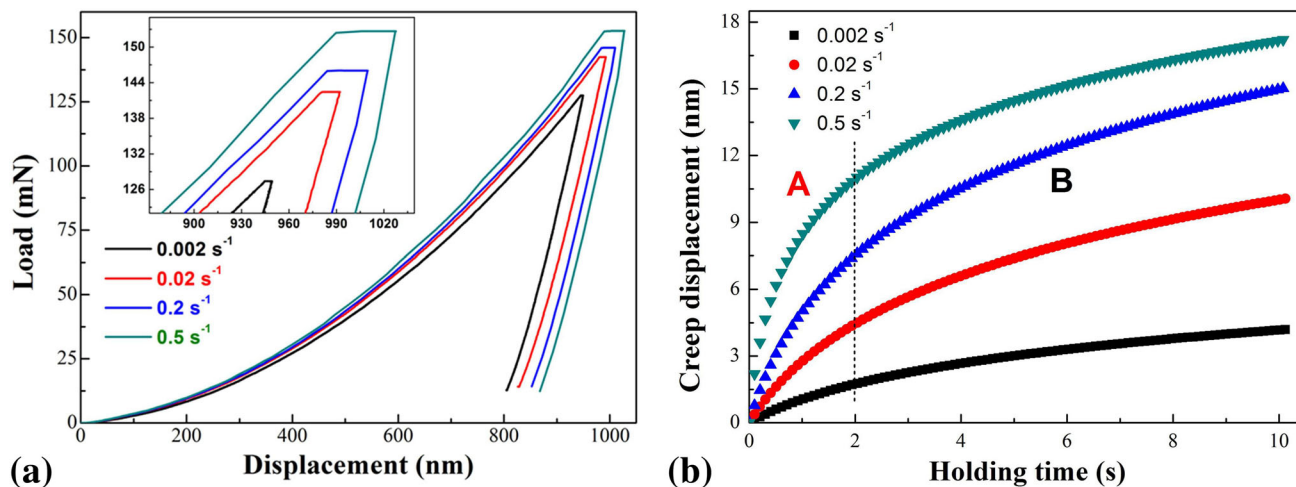

Fig. 2 Representative load-displacement curves (a) and creep displacements during the holding stage (10 s) obtained at four different indentation strain rates (b) for the present alloy with a depth limit of 1000 nm. The inset in (a) is the magnified portion at the approximate indentation depth of 900 nm

Fig. 2(b). At A stage, the creep rate declines rapidly, but the creep depth increases dramatically. Then, the creep curves almost linearly ascend with time during B stage (Ref 15). Indeed, the creep behavior is dominated by the strain hardening at A stage and then, transits into the dislocation migration viscous stage. The strain-hardening effect dominates in a very short time, while the visco-plastic stage accounts for most of the creep stage during the holding period (Ref 35).

For the sake of vividly elucidating the deformation mechanisms for the current alloy after nanoindentation, in-situ scanning images of the indent at the strain rate of $0.02 \ s^{-1}$ with a depth limit of 1000 nm using a Berkovich tip are typically exhibited in Fig. 3. The sample surface uplifts owing to the material pileup, which can be clearly observed around the indent. As an important phenomenon of plastic deformation, the significant pileup of the present alloy suggests that a heavy and highly localized plastic deformation occurs during nanoindentation (Ref 36).

For a perfect Berkovich diamond indenter, the projected contact area, A_c, can be determined as (Ref 37):

$$A_c = 24.56 \, h_c^2, \tag{Eq 1}$$

where h_c is the contact depth and estimated by the following equation (Ref 38):

$$h_c = h_{max} - \varepsilon \frac{P_{max}}{S}, \tag{Eq 2}$$

where h_{max} is the maximum indentation depth, $\varepsilon = 0.75$ is a constant for the Berkovich indenter, and P_{max} is the corresponding maximum load, and S is the elastic contact stiffness. Based on CSM technique, the contact stiffness, S, can be computed as follows (Ref 20):

$$S = \left[\frac{1}{\left(F_{amp}/h_{amp}\right) \cos \phi - m\omega^2} \frac{1}{K_f} \right], \tag{Eq 3}$$

where F_{amp} is the amplitude of harmonic excitation force, h_{amp} is response displacement amplitude (~ 2 nm), φ is the phase shift (Ref 37), $\omega = 2\pi f$ is the angular frequency ($f = 45$ Hz), K_s, m, and K_f are the spring contact in the perpendicular orientation, mass of the indenter, and frame stiffness, respectively. The elementary relations of H and E can be derived as follows (Ref 38):

$$H = \frac{P_{max}}{A_c} \tag{Eq 4}$$

$$E_r = \frac{\sqrt{\pi}}{2\beta} \cdot \frac{S}{\sqrt{A_c}}, \tag{Eq 5}$$

where E_r is the reduced elastic modulus, and $\beta = 1.034$ is the shape constant of Berkovich tip. Since E_r is used to account

for the combined response of the indenter and the sample, the elastic modulus of the test material, E, can be calculated from E_r using (Ref 38):

$$\frac{1}{E_r} = \frac{1 - v^2}{E} + \frac{1 - v_i^2}{E_i}, \tag{Eq 6}$$

where v and E are the Poisson's ratio and elastic modulus of the sample respectively, and E_i and v_i are the elastic modulus and Poisson's ratio for the indenter, respectively. For the diamond indenter, $E_i = 1141$ GPa and $v_i = 0.07$ are employed (Ref 20, 39).

According to aforementioned instrumented indentation testing methods (Ref 20, 21), the mechanical properties obtained from the load-displacement curves during nanoindentation at different indentation strain rates, including the maximum depth, h_{max}, elastic modulus, E, and hardness, H, are summarized in Table 1. It is noted that the elastic modulus remains unchanged at different strain rates, showing the less dependence of the strain rate, as shown in Fig. 4(a). In terms of the small change of elastic modulus, it can be attributed to anisotropy in crystalline properties under various strain rates during nanoindentation (Ref 37). It is revealed in Fig. 4(a) that the hardness increases with the increase of strain rates, which coincides well with the variation at different strain rates under the same indentation depth, as exhibited in Fig. 4(b). In addition, it is interesting to note that the hardness decreases with increasing the indentation depth, as shown in Fig. 4(b). It can be explained by the ISE in nanohardness that the reduction of the indent size results in both increasing hardness and decreasing plasticity (Ref 40). The ISE can be explicated by the deformation mechanism of geometrically necessary dislocations (GNDs), where the density of dislocations increases as the indentation depth decreases and dislocations spread over smaller slip circles, thus, giving rise to the ISE of hardness for crystalline materials (Ref 40).

In order to elaborate the effect of Al concentration on mechanical performance in the $Al_xCoCrFeNi$ alloy system, the comparison analysis is required. Figure 5 exhibits the comparison in the modulus and hardness of $Al_xCoCrFeNi$ alloy system (Ref 36, 41) with different x values by nanoindentation with a strain rate of $0.2 \ s^{-1}$. As shown in Fig. 5(a), the modulus of the three alloys increases with the increase of Al content. As reported previously (Ref 42), the binding force between elements increases with the more negative H_{mix} (the enthalpy of mixing), macroscopically dominating the modulus of the metallic materials. It is noted that the absolute value of enthalpy of mixing increases with the more Al concentration (Ref 42), which is in agreement well with the comparison results as shown in Fig. 5(a). It is worth noting that the hardness of AlCoCrFeNi alloy is obviously greater than that of $Al_xCoCrFeNi$ ($x = 0.3, 0.5$) HEAs, as exhibited in Fig. 5(b). The main

Table 1 Mechanical properties of AlCoCrFeNi alloy

	1000 nm		
Depth limitStrain rate, s^{-1}	h_{max}, nm	E, GPa	H, GPa
0.002	975.67	230.47	7.90
0.02	994.64	230.66	8.52
0.2	1009.79	233.84	8.91
0.5	1024.68	226.001	9.49
Average	1001.23	230.24	8.71
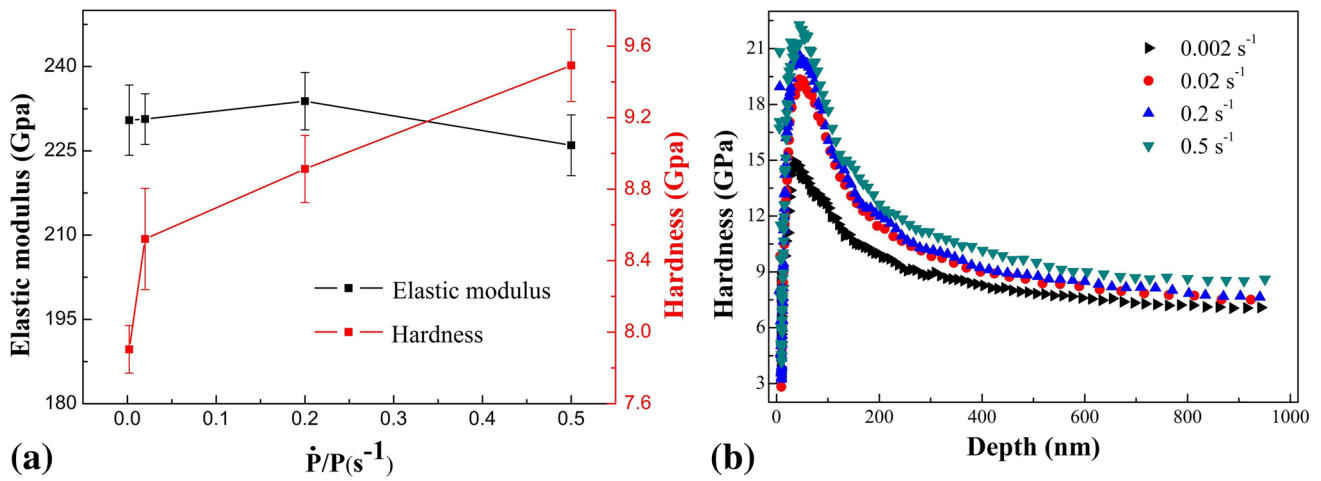
Fig. 4 Representative average values and standard deviation of modulus and hardness (a) and corresponding hardness-depth curves under different indentation strain rates (b) of the AlCoCrFeNi alloy
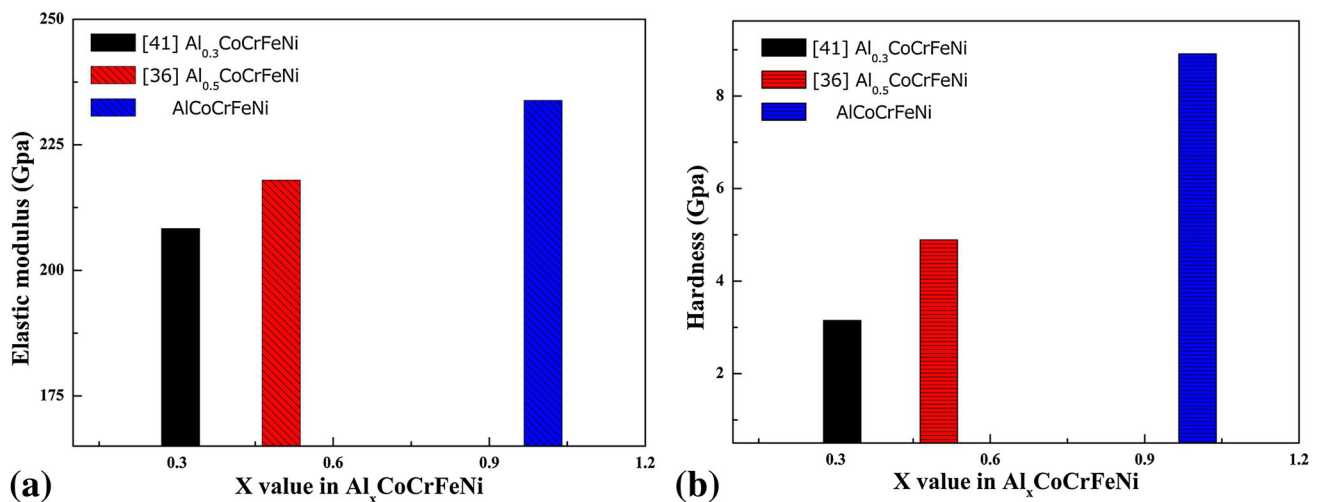
Fig. 5 Comparison in the modulus and hardness of Al$_x$CoCrFeNi alloy system with different x values: (a) modulus of Al$_x$CoCrFeNi and (b) hardness of Al$_x$CoCrFeNi

reason for the larger hardness with increasing Al concentration in multi-component alloys lies in the solid solution strengthening, which can be utilized to improve the strength of metal materials as an alloying effect (Ref 43). For the Al$_x$CoCrFeNi alloy system, the four components Co, Cr, Fe, and Ni have equiatomic ratio and have the same possibility to occupy the lattice sites (Ref 18). As the Al with larger atomic radius occupies the lattice sites, the lattice distortion energy will increase significantly and the effect of solid solution strengthening is enhanced, thus the hardness greatly increases, with increasing the Al concentration (Ref 1).

4. Conclusions

In conclusion, an instrumented nanoindentation has been utilized to investigate the deformation behavior of the AlCoCrFeNi alloy at different indentation strain rates. It is revealed that the creep behavior of the present alloy shows significant strain rate sensitivity. In addition, the severe pileup

around the indent suggests that a highly localized plastic deformation occurred during the nanoindentation. The elastic modulus remains unchanged under different indentation strain rates, demonstrating that the elastic modulus of the alloy is not only less loading rate dependent (Ref 19) but also less strain rate dependent. However, the hardness of the alloy is strain rate dependent which decreases with increasing indentation depth due to the ISE in nanohardness. Moreover, compared with the Al$_x$CoCrFeNi ($x = 0.3, 0.5$), the AlCoCrFeNi HEAs has a greater modulus and hardness due to its higher negative enthalpy of mixing related to the atomic binding force, and the solid solution strengthening induced by the lattice distortion, respectively.

References

1. Y.J. Zhou, Y. Zhang, Y.L. Wang, and G.L. Chen, Solid Solution Alloys of AlCoCrFeNiTi$_x$ with Excellent Room-Temperature Mechanical Properties, *Appl. Phys. Lett.*, 2007, **90**, p 181904

2. C.Y. Hsu, J.W. Yeh, S.K. Chen, and T.T. Shun, Wear Resistance and High-Temperature Compression Strength of Fcc CuCoNiCrAl$_{0.5}$Fe Alloy with Boron Addition, *Metall. Mater. Trans. A*, 2004, **35**, p 1465

3. Y. Zhang, Y.J. Zhou, J.P. Lin, G.L. Chen, and P.K. Liaw, Solid-Solution Phase Formation Rules for Multi-component Alloys, *Adv. Eng. Mater.*, 2008, **10**, p 534

4. Y. Zhang, T.T. Zuo, Z. Tang, M.C. Gao, K.A. Dahmen, P.K. Liaw, and Z.P. Lu, Microstructures and Properties of High-Entropy Alloys, *Prog. Mater Sci.*, 2014, **61**, p 1

5. J.W. Yeh, Y.L. Chen, S.J. Lin, and S.K. Chen, High-Entropy Alloys—a New era of Exploitation, *Mater. Sci. Forum*, 2007, **560**, p 1

6. P.K. Huang, J.W. Yeh, T.T. Shun, and S.K. Chen, Multi-principal-Element Alloys with Improved Oxidation and Wear Resistance for Thermal Spray Coating, *Adv. Eng. Mater.*, 2004, **6**, p 74

7. M.C. Gao, B. Zhang, S.M. Guo, J.W. Qiao, and J.A. Hawk, High-Entropy Alloys in Hexagonal Close-Packed Structure, *Metall. Meter. Trans. A.*, 2015, doi:10.1007/s11661-015-3091-1

8. J.W. Yeh, S.K. Chen, J.Y. Gain, S.J. Lin, T.S. Chin, T.T. Shun, C.H. Tsau, and S.Y. Chang, Formation of Simple Crystal Structures in Cu-Co-Ni-Cr-Al-Fe-Ti-V Alloys with Multi Principal Metallic Elements, *Metall. Meter. Trans. A.*, 2004, **35A**, p 2535

9. R.A. Swalin, *Thermodynamics of Solids*, 2nd ed., E. Burke, B. Charmers, J.A. Krumhansl, Eds., Wiley, New York, 1991, p 21

10. F.R. de Boer, Cohesion in Metals: Transition Metal Alloys, F.R. de Boer and D.G. pettifor, Eds. Elsevier, New York, 1988

11. Y.J. Zhou, Y. Zhang, Y.L. Wang, and G.L. Chen, Microstructure and Compressive Properties of Multicomponent Al$_x$(TiVCrMnFeCoNiCu)$_{100-x}$ High-Entropy Alloys, *Mater. Sci. Eng. A*, 2007, **454-455**, p 260

12. Y.P. Wang, B.S. Li, M.X. Ren, C. Yang, and H.Z. Fu, Microstructure and Compressive Properties of AlCrFeCoNi High Entropy Alloy, *Mater. Sci. Eng. A*, 2008, **491**, p 154

13. T.T. Shun and Y.C. Du, Microstructure and Tensile Behaviors of FCC Al0.3CoCrFeNi High Entropy Alloy, *J. Alloys Compd.*, 2009, **479**, p 157

14. V. Dolique, A.L. Thomann, P. Brault, Y. Tessier, and P. Gillon, Thermal Stability of AlCoCrCuFeNi High Entropy Alloy Thin Films Studied by In-Situ XRD Analysis, *Surf. Coat. Technol.*, 1989, **2010**, p 204

15. Y. Ma, G.J. Peng, D.H. Wen, and T.H. Zhang, Nanoindentation Creep Behavior in a CoCrFeCuNi High-Entropy Alloy Film with Two Different Structure States, *Mater. Sci. Eng. A*, 2015, **621**, p 111

16. B.S. Murty, J.W. Yeh, and S. Ranganathan, *High Entropy Alloys*, Butterworth-Heinemann, London, 2014

17. D.B. Miracle, Critical Assessment 14: High Entropy Alloys and Their Development as Structural Materials, *Mater. Sci. Technol*, 2015, **31**, p 1244

18. W.R. Wang, W.L. Wang, S.C. Wang, Y.C. Tsai, C.H. Lai, and J.W. Yeh, Effects of Al Addition on the Microstructure and Mechanical Property of Al$_x$CoCrFeNi High-Entropy Alloys, *Intermetallics*, 2012, **26**, p 44

19. Z.M. Jiao, S.G. Ma, G.Z. Yuan, Z.H. Wang, and H.J. Qiao, Plastic Deformation of Al$_{0.3}$CoCrFeNi and AlCoCrFeNi High-Entropy Alloys Under Nanoindentation, *J. Mater. Eng. Perform.*, 2015, **24**(8), p 3077

20. W.C. Oliver and G.M. Pharr, An Improved Technique for Determining Hardness and Elastic Modulus Using Load and Displacement Sensing Indentation Experiments, *J. Mater. Res.*, 1992, **7**, p 1564

21. W.C. Oliver and G.M. Pharr, Measurement of Hardness and Elastic Modulus by Instrumented Indentation: Advances in Understanding and Refinements to Methodology, *J. Mater. Res.*, 2004, **19**, p 3

22. M. Dao, N. Chollacoop, K.J. Van Vliet, T.A. Venkatesh, and S. Suresh, Computational Modeling of the Forward and Reverse Problems in Instrumented Sharp Indentation, *Acta Mater.*, 2001, **49**, p 3899

23. S. Suresh and A.E. Giannakopoulos, A New Method for Estimating Residual Stresses by Instrumented Sharp Indentation, *Acta Mater.*, 1998, **46**, p 5755

24. B.N. Lucas and W.C. Oliver, Indentation Power-Law Creep of High-Purity Indium, *Metall. Mater. Trans. A*, 1999, **30**, p 601

25. J.B. Pethica and W.C. Oliver, Tip Surface Interactions in STM and AFM, *Phys. Scr.*, 1987, **19**, p 61

26. W.C. Oliver, J.B. Pethica, Methods for Continuous Determination of the Elastic Stiffness of Contact Between Two Bodies. 1989, US Patent 4848141

27. G.M. Pharr, W.C. Oliver, and F.R. Brotzen, On the Generality of the Relationship Among Contact Stiffness, Contact Area, and Elastic Modulus During Indentation, *J. Mater. Res.*, 1992, **7**, p 613

28. C.A. Schuh and T.G. Nieh, A Nanoindentation Study of Serrated Flow in Bulk Metallic Glasses, *Acta Mater.*, 2003, **51**, p 87

29. C.A. Schuh, A.C. Lund, and T.G. Nieh, New Regime of Homogeneous Flow in the Deformation Map of Metallic Glasses: Elevated Temperature Nanoindentation Experiments and Mechanistic Modeling, *Acta Mater.*, 2011, **59**, p 7480

30. W.H. Poisl, W.C. Oliver, and B.D. Fabes, The Relationship Between Indentation and Uniaxial Creep in Amorphous Selenium, *J. Mater. Res.*, 1995, **10**, p 2024

31. Z. Tang, O.N. Senkov, C.M. Parish, C. Zhang, F. Zhang, L.J. Santodonato, G.Y. Wang, G.F. Zhao, F.Q. Yang, and P.K. Liaw, Tensile Ductility of an AlCoCrFeNi Multi-phase High-Entropy Alloy Through Hot Isostatic Pressing (HIP) and Homogenization, *Mater. Sci. Eng. A*, 2015, **647**, p 229

32. W.B. Li, J.L. Henshall, R.M. Hooper, and K.E. Easterling, The Mechanisms of Indentation Creep, *Acta Metall. Mater.*, 1991, **39**, p 3099

33. S.A. Syed Asif and J.B. Pethica, Nanoindentation Creep of Single-Crystal Tungsten and Gallium Arsenide, *Philos. Mag. A*, 1997, **76**, p 1105

34. B.G. Yoo, K.S. Kim, J.H. Oh, U. Ramamurty, and J.I. Jang, Room Temperature Creep in Amorphous Alloys: Influence of Initial Strain and Free Volume, *Scr. Mater.*, 2010, **63**, p 1205

35. Z.J. Wang, S. Guo, Q. Wang, Z.Y. Liu, J.C. Wang, Y. Yang, and C.T. Liu, Nanoindentation Characterized Initial Creep Behavior of a High-Entropy-Based Alloy CoFeNi, *Intermetallics*, 2014, **53**, p 183

36. Z.M. Jiao, M.Y. Chu, H.J. Yang, Z.H. Wang, and J.W. Qiao, Nanoindentation Characterized Plastic Deformation of a Al$_{0.5}$CoCrFeNi High Entropy Alloy, *Mater. Sci. Technol.*, 2015, **31**, p 1244

37. A.C. Fischer-Cripps, *Introduction to Contact Mechanics*, Springer, New York, 2000

38. J.E. Zorzi and C.A. Perottoni, Estimating Young's Modulus and Poisson's ratio by Instrumented Indentation Test, *Mater. Sci. Eng. A*, 2013, **574**, p 25

39. G. Simmons and H. Wang, *Single Crystal Elastic Constants and Calculated Aggregate Properties*, MIT Press, New York, 1971

40. Y.V. Milman, A.A. Golubenko, and S.N. Dub, Indentation Size Effect in Nanohardness, *Acta Mater.*, 2011, **59**, p 7480

41. S.G. Ma, S.F. Zhang, J.W. Qiao, Z.H. Wang, M.C. Gao, Z.M. Jiao, H.J. Yang, and Y. Zhang, Superior High Tensile Elongation of a Single-Crystal CoCrFeNiAl$_{0.3}$ High-Entropy Alloy by Bridgman Solidification, *Intermetallics*, 2014, **54**, p 10450

42. X. Yang and Y. Zhang, Prediction of High-Entropy Stabilized Solid-Solution in Multi-component Alloys, *Mater. Chem. Phys.*, 2012, **132**, p 233

43. L.M. Surhone, M.T. Timpledon, and S.F. Marseken, *Solid Solution Strengthening*, Betascript, UK, 2010